Structure Diagnostics Review

Chuck Rino

May 15, 2026

1 Introduction

This note is a review of diagnostic BP-IP in response to a number of comments, mainly by Charlie, and ongoing or planned parallel efforts by Dmytro, Luca, and Andrew. The BP-IP analysis presented in our recent paper and the additional analysis summarized in this note provide a template for moving beyond morphological studies based on the standard scintillation measures, $S4$, σ_ϕ, and $ROTI$.

2 Critical Assumptions

The critical assumptions can be summarized as follows:

1. The intercepted structure can be visualized as a random collection of elongated *magnetic-field-aligned* striations. The size distribution of the striations is defined by striation profile intersections with or containment within two-dimensional slice planes cutting across the striations. This implies that defining statistical measures are two-dimensional.

2. An evolving complex field intercepting the structure can be decomposed into a spectrum of plane waves that subtend a narrow range of propagation angles. Under this assumption multiple phase screen (MPS) simulations capture the essential propagation effects that must be accommodated.

3. Processing is performed over segments with a predetermined length. The segment structure is characterized by statistical measures generated from samples within the segments. Sufficient homogeneity to support definitive statistical measures must verified.

4. The observed temporal structure is the result of incremental integration over a translating propagation path intercepting structure that evolves slowly enough to be spatially invariant over the measurement interval.

From assumption 1 the stochastic component of the evolving two-dimensional structure is captured by a one-dimensional slice through the evolving structure. Without loss of generality the x axis can be aligned with the propagation

direction. Propagation effects are captured by a two-dimensional projection $\Delta N_e(x, y)$. From assumptions 2 and 4, path-integrated phase

$$\phi(y) = 2\pi K/f \int_0^L \Delta N_e(x, y)dx, \tag{1}$$

where

$$K = r_e c/(2\pi) \times 10^{16}, \tag{2}$$

is sufficient to characterize the evolving complex field. Complex field realizations can be generated by using the MPS method. If $\Delta N_e(x, y)$ is characterized by a two-dimensional homogeneous stochastic process it follows by direct computation from (1) that

$$\Phi_\phi(\kappa_y) = (2\pi KL/f)^2 \int \frac{\sin^2(\kappa_x L/2)}{(\kappa_x L/2)^2} \Phi_{\Delta N_e}(\kappa_x, \kappa_y) \frac{d\kappa_x}{2\pi}, \tag{3}$$

where $\Phi_{\Delta N_e}(\kappa_x, \kappa_y)$ is the spectral density function and κ_γ is a spatial wavenumber component with units $2\pi/l$. Formally, $\Phi_{\Delta N_e}(\kappa_x, \kappa_y)$ is the average intensity of the two-dimensional spatial Fourier decomposition of $\Delta N_e(x, y)$.

The anisotropy introduced by propagation-paths intercepting *locally parallel* striations at oblique angles is incorporated by assuming that countours of constant correlation or spectral intensity are characterized by projecting and scaling isotropic forms. Formally,

$$\Phi_{\Delta N_e}(\kappa_x, \kappa_y) = G\Phi_{\Delta N_e}(\kappa_s), \tag{4}$$

where κ_s is the magnitude of the transformed spatial wavenumber transformed as follows

$$\boldsymbol{\kappa}_s = \boldsymbol{\kappa}^T C \boldsymbol{\kappa}. \tag{5}$$

The factor G preserves the defining relation

$$\left\langle \Delta N_e(x, y)^2 \right\rangle = \iint \Phi_{\Delta N_e}(\kappa_x, \kappa_y) \frac{d\kappa_x}{2\pi} \frac{d\kappa_y}{2\pi}. \tag{6}$$

If the structure is uncorrelated along the propagation path, the following approximation can be used:

$$\Phi_\phi(\kappa_y) = (2\pi K/f)^2 L\Phi_{\Delta N_e}(0, \kappa_y). \tag{7}$$

Repeating the electron density variance computation

$$\left\langle \phi(y)^2 \right\rangle = (2\pi K/f)^2 L \int \Phi_{\Delta N_e}(0, \kappa_y) \frac{d\kappa_y}{2\pi}. \tag{8}$$

A representative isotropic two-component structure can be defined in terms of four structure parameters, GC_s, η_1, η_2, and $\overline{\kappa}_0$ as follows:

$$\Phi_{\Delta N_e}(\kappa_s) = GC_s \begin{cases} {\kappa_s}^{-\eta_1}, & \kappa_s \leq \overline{\kappa}_0 \\ ({\overline{\kappa}_0}^{\eta_2 - \eta_1}) {\kappa_s}^{-\eta_2}, & \kappa_s > \overline{\kappa}_0 \end{cases}. \tag{9}$$

However, the radial power-law index differs from the coordinate index. For interpreting phase spectra we use the form

$$\Phi_\phi(\kappa_y) = C_p \begin{cases} {\kappa_y}^{-p_1}, \ \kappa_y \leq \kappa_0 \\ ({\kappa_0}^{p_2-p_1})\kappa_y^{-p_2}, \ \kappa_y > \kappa_0 \end{cases}, \tag{10}$$

where

$$C_p \sim (2\pi K/f)^2 \, \overline{C}_s.$$

The measured IPE parameter C_p at a specified frequency defines an aggregate in-situ structure measure $\overline{C}_s$, which can be further refined from the known geometry and estimates of the disturbed region extend. The break scale, $\overline{\kappa}_0$, also changes with geometry. Following the relation for a single power law, we expect the radial and component spectral indices to be related as $\eta = p - 1$. The approximations can be verified by numerical integration over defined spatial wavenumber ranges with defining parameters specified. The ramifications of converging magnetic field lines must be evaluated.

3 Temporal-to-spatial conversion

Statistical measures require a degree of homogeneity formally referred to as ergodicity, meaning that statistical measures can be estimated with operations applied to series. For homogeneous segments a single effective scan velocity, v_{veff}, translates time to distance as

$$y = v_{\text{veff}}(t - t_0). \tag{11}$$

Formally, v_{veff} is the projection of the penetration point velocity relative to the structure. For a specified penetration point height, receiver and satellite locations determine the path translation contribution. The drift contribution is an unknown offset.

Upon implementing back propagation (BP) there is an effective scan velocity that accommodates the spatial wavenumber range supported by the resolved Doppler frequency range. The definition

$$v_{\text{veff}} = \pi f_{\text{Nyq}}/k. \tag{12}$$

equates the Nyquist frequency and the largest contributing spatial frequency. The length of the segment determines the smallest contributing spatial frequency. The *effective* scale and spatial frequency ranges are

$$y = v_{\text{veff}} \, (t - t_0) \tag{13}$$

$$\kappa_y = 2\pi f_{\text{Dop}}/v_{\text{veff}}. \tag{14}$$

The captured scale range can be verified by comparing estimated and theoretically predicted measures.

Ideally, BP would be applied to the complex scintillation imparted to the signal after propagation through a disturbed region. However, the transmitted signal is subject to path-loss and antenna gain variations as well as noise, interference, and multipath. Preprocessing operations include estimation of the noise level and estimation of the imposed signal variation, which is used to detrend the intensity. The detrending operation imposes a normalization that sustains a constant average intensity over the processing interval. Signal phase is dominated by a range-rate-induced Doppler shift, which can be removed for total electron content (TEC) measurement by using a frequency-scaled phase difference. The preprocessing operations are described in [1] and the cited references.

The critical operations for structure diagnostics are phase extraction and irregularity parameter estimation (IPE). The strict application of phase-screen equivalence attributes all the structure development to free propagation. However, it has been demonstrated that phase-screen results are statistically equivalent to MPS results if the equivalent phase screen is placed at the center of the structure region. Figure 1, which was taken from [2], shows a comparison of MPS, which is denoted PWE in the figure, and an equivalent phase-screen generated by placing the path-integrated structure at the center of the disturbed region. This particular example incorporated truncated field-aligned structure.

4 Back Propagation

Reconstructing the field at the BP intensity variance minimum effectively generates a statistically equivalent phase screen field. Simulation examples in [1] showed that back propagation identifies a central point within the structured region. Figure 2 , which is taken from [1], is an MPS simulation verifing that the BP reconstructed phase can be used to estimate the incremental phase that generated complex field in the measurement plane. The extent to which the disturbance and the incremental turbulent strength can be varied has been explored for occultation diagnostics [3]. Extreme scintillation presents additional challenges due to degradation of the phase extracted from the BP complex field. Reconstructing the height of the penetration point at the BP range provides a check on the integrity of the computation.

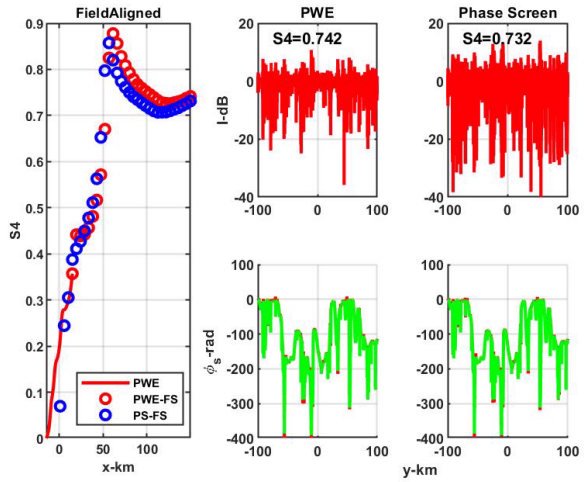

Figure 1: Example of phase screen (red) and MPS(PWE) equivalence.

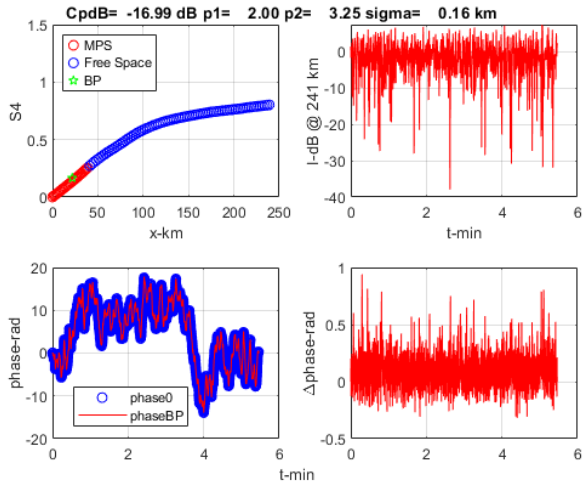

Figure 2: BP-IP applied to MPS realization.

5 Imposed Magnetic Field Curvature Structure Variation

Because magnetic field lines are curved there is a convergence of field-lines initiated in the equatorial plane. This can be seen in Figure 3 which shows uniformly sampled meridional and equatorial plane slices of an EPB simulation at 50 min. The left-hand frame shows meridian-plane structure. The right-hand frame shows equatoral-plane structure. Although the two frames have equal height sampling and a common axis at $y = z = 0$, the zonal y extent is much smaller than the meriodinal z extent, which implies different horizontal structure at common altitudes. This is verified in Figure 3. The upper frame shows a representative horizontal scan of the equatoral-plane structure at 509 km. The second frame shows the periodogram SDF estimate (red). Structure parameter estimates were estimated by applying irregularity parameter estimation (IPE) to measured periodogram SDF estimates as described in [4]. The analytic SDF form (10) evaluated with the IPE parameters was overlaid on the periodogram SDF (green). The good agreement between the measured SDFs and the analytic forms validate the IPE procedure. The lower frames in 3 show identical summaries for the meridional-plane scan at 509 km.

To guide data interpretation, field-line tracing to identify potential paths from equatorial-plane structure to penetration-point samples. It is noteworthy that definitive field-line paths from arbitrary penetration point paths depend on proximity to the geomatic equator and the direction of the penetration point trajectory. The IGRF magnetic field model generates magnetic-field direction and intensity at any specified GPS point. With the direction specified as eastward, northward, and upward incremental projections of the magnetic field are readily constructed. Because of the slow variation of the field large steps can be used for efficient computation.

Figure 5 shows a trajectory southward from a station location indicated by the red pentagram, which is very close to an ideal cross-field sampling. Such trajectories would be expected to accurately reproduce the defining structure in the equatorial meridian plane indicated by an altitude inflection indicated by red pentagrams. The mapping would be largely independent of altitude. Figure 6 shows effect of changing the direction of the penetration point trajectory. The sampled trajectories capture altitude-dependent larger scale structure, which can explain the results summarized in Figures 3 and 4. Calculating the potential structure distortion could be realized most directly by using configuration-space realizations as described in [5].

We conclude noting that there is no guarantee that paticular measurement will map to a defining equatorial plane intercept within the height range of significant structure electron density. We identify two criteria for definitive EPB structure diagnostics. First the back-propagation range must identify a structure height commensurate with detectable structure strength. Second, the field line from the penetration point must intercept the equatorial plane in the same height range.

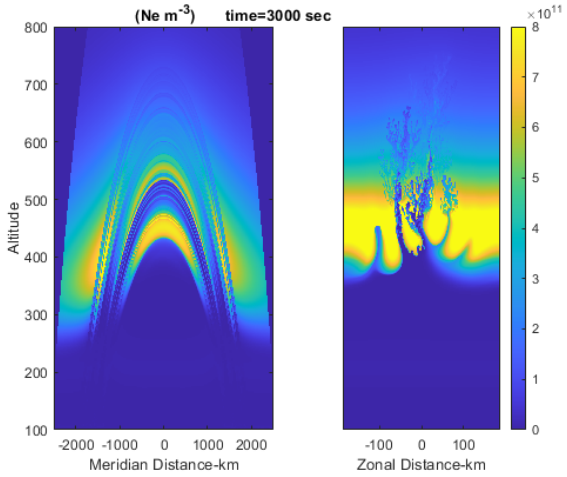

Figure 3: Meridian plane (left) and equatorial plane (right) displays of simulated EPB electron density structure at 50 min.

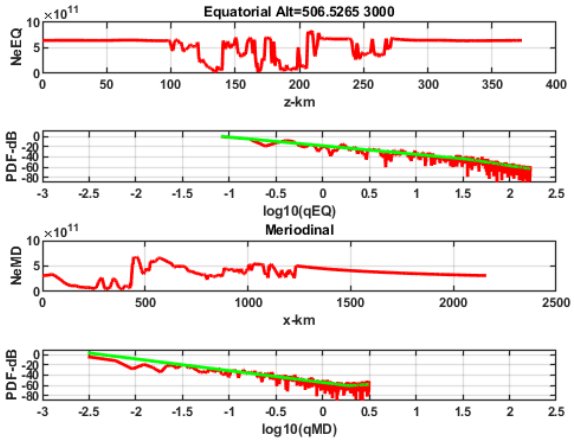

Figure 4: Upper frame shows horizontal scan of equatorial plane structure at 509 km (red). Second frame shows measured SDF (red) and IPE SDF overlaid (green). Lower frames summarize the larger span meridian plane structure.

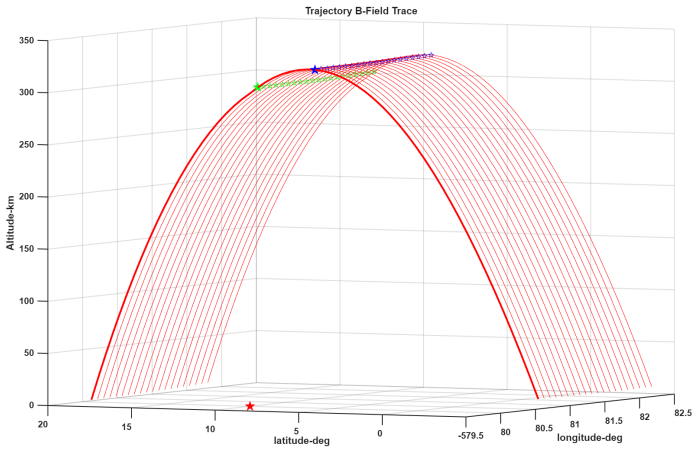

Figure 5: Field-line trajectories (red) from east-west penetration points identified by green pentagrams. Altitude inflection points are indicated by blue pentagrams.

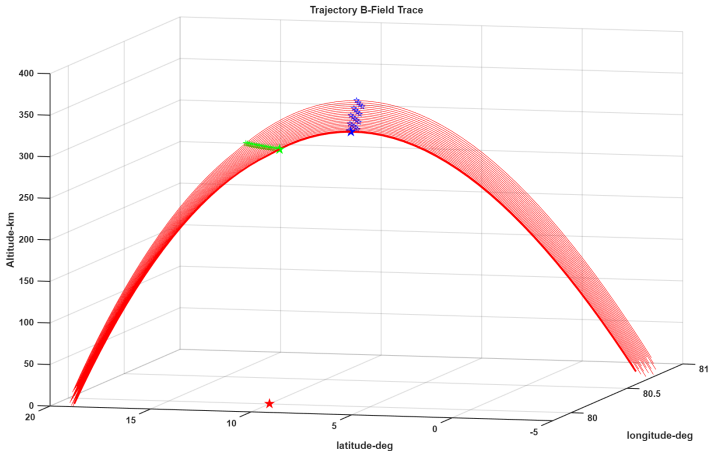

Figure 6: Field-line trajectories (red) from north-south penetration points identified by green pentagrams.

6 Representative Examples

Diagnostic examples summarized in [1] introduced BP-IPE as a scintillation data analysis procedure for characterizing the electron density structure. From EPB simulations a two-component inverse-power-law SDF with $p_1 < p_2$ was expected. Instead, a preponderance of structure with $p_1 \geqq p_2$, often with $p_1 > 3$, was observed. The results were obtained by applying BP-IPE processing to contiguous 5-min data segments after preprocessing operations to extract the imparted scintillation complex modulation. A 5-min segmentation for processing was used to accommodating extreme scintillation. However, from a strict analysis viewpoint it is desirable to use the largest processing interval the data will support.

Regarding phase, the geometric Doppler imposed by changing range is usually dominant. For TEC measuremen the geometric Doppler contribution can be removed by subtracting frequency-scaled phase measurements at two freequenies. However, our interest is in smaller scale structure, which can be extracted from single-frequency measurements. Geometric Doppler imposes a large-scale phase variation limit in much the same way that antenna pattern and path-loss variations impose large-scale intensity variation limits. Additionally, phase noise comes mainly from the receiver oscillator. It was found that IPE applied to single-frequency phase measurements provided identification of the phase noise starting at the break frequency. With the noise range identified a second IPE application over a truncated Doppler frequency range isolates phase structure of interest.

Regarding BP, calculating the penetration-point height using the corrected range BP range provides a check on the BP operation. Segments with penetration point intercepts between 200 to 800 km are designated BP_OK. Field line tracing from each ionosphere penetration point was used to identify a connection to the equatorial plane within a specified altitude structure range. Each BP_OK segment is identified as EPB if $p_1 < p_2$ and $p_2 - p_1 > 0.5$ or as PPB if $p_2 < p_1$ and $p_1 - p_2 > 1$. Otherwise the segment is identified as P12 indicating that the structure is indistinguishable from a single power law. Additionally, BP_OK segments with an equatorial plane intercept are designated EX_OK. No prior assessment of geometric structure distortion is made.

Table 1 summarizes the results. The number of segments process for each station is listed together with a BP_OK and EX_OK breadown. The Hong Kong segments from 61 passes recorded over a one-year period were processed. Lampedusa and Malindi segments from 11 and 8 passes recorded over two-day periods were processed. Observations of EPB structure and PPB structure were generally clustered within single passes intermixed with P12 segments.

Figure 7 shows the geographic location of the stations relative to the magnetic equator. The fact that all of the Malindi passes had EX_OK geometries is attributed to the proximity of the Malindi station to the magnetic equator. The summarized results in Table 1 are a refinement of the structure summaries in [1]. The P12 category isolates single inverse power law segments. Phase fitting refinements changed the EPB and PPB segment counts by small amounts.

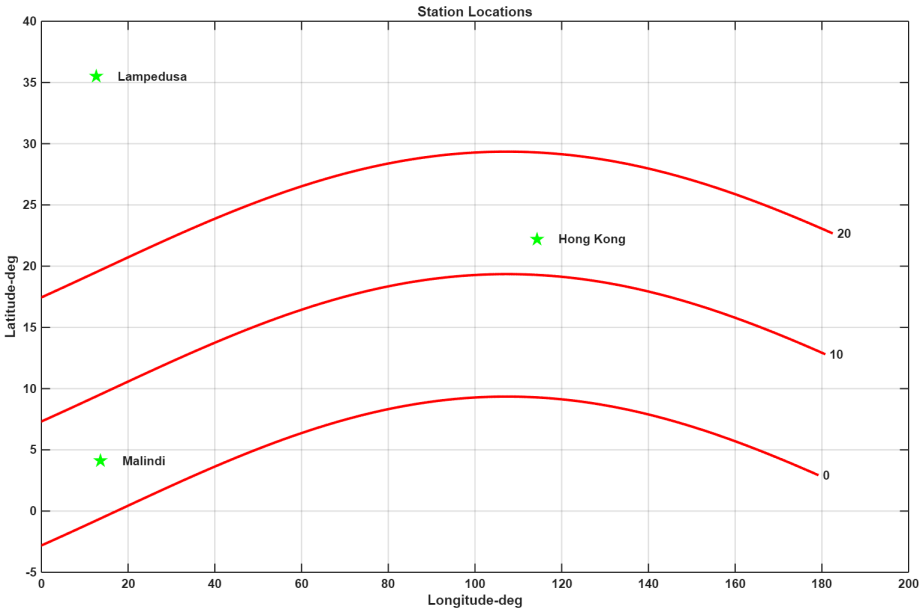

Figure 7: Station locations with consant magnetic field lines at the indicated geomagnetic latitudes.

Segment Structure Summary

Hong Kong 1159 segs

	EPB	PPB	P12
BP_OK=722	85	314	323
EX_OK=193	32	88	73

Lampedusa 586 segs

	EPB	PPB	P12
BP_OK= 321	7	144	170
EX_OK= 11	0	4	7

Malindi 646 segs

	EPB	PPB	P12
BP_OK= 377	9	228	140
EX_OK= 377	9	228	140

Table 1

Only a small fraction of the processed segments from each station could be identified definitively with the expected EPB structure evolution. Figure 8 summarizes a Hong Kong pass with a particularly well-defined structure evolution. The field lines (red) passing through penetration points are identified with green pentagrams for EPB segments and green circles for PPB segments. The penetration point progression is from left to right. The measured scintillation (not shown) increases to saturation and then recedes. The results can be interpreted as a propagation path sweeping throug developing EPB structure. The two PPB segments captured in 8 correspond to less disturbed segments.

Figure 9 shows an unfavorable Hong Kong geometry with PPB segments possible caused by geometric distortions as observed in the simulated EPB meridian plane structure. More disturbed segments with both EPB and PPB structure can be found.

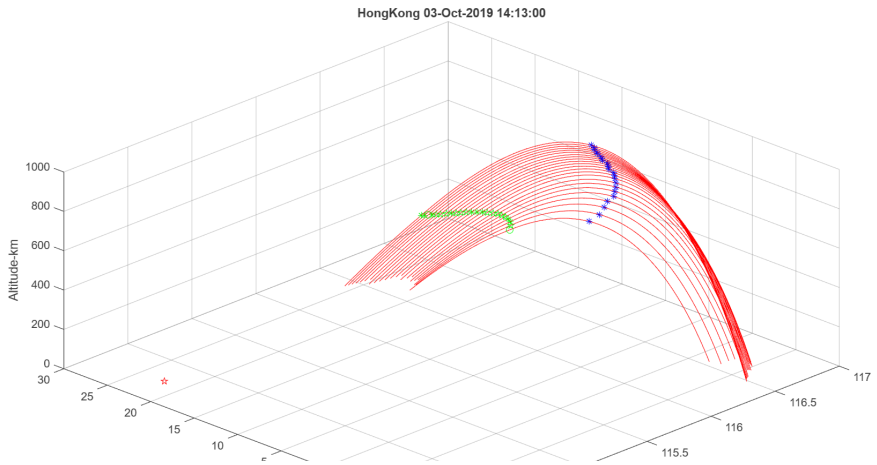

Figure 8: Hong Kong pass summary consistent with intercepting EPB structure.

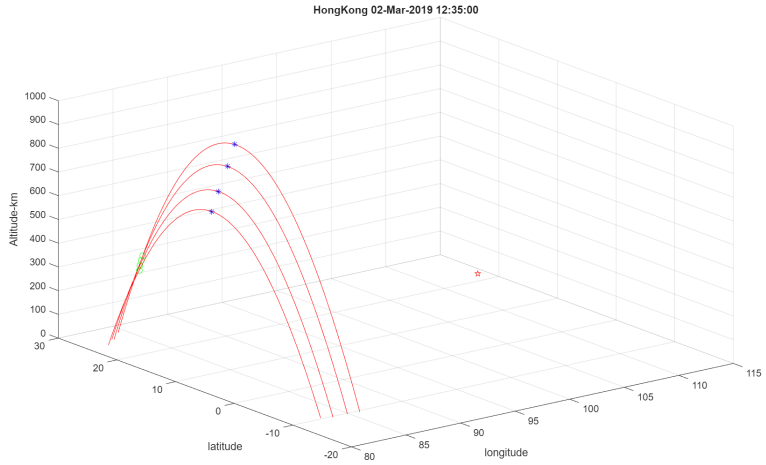

Figure 9: Summary of Hong Kong pass segments with unfavorable geometry showing PPB structure.

Although there is evidence of geometric distortion the overwhelming number of PPB segments is difficult to reconcile with with EPB simulations. Moreover, the same PPB occurrence patterns are observed. This is most readily demonstrated when the data are organized by perturbation strength. Extreme low-latitude scintillation is observed with well known regular diurnal and seasonal occurrence patterns. The Hong Kong data was acquired during a period of moderate solar activity. Although stronger scintillation was expected and observed during the more recent Lampedusa and Malindi observations the fractional occurrece of EPB and PPB segments were similar.

From phase-screen theory we know that perturbation strength is ordered by the U parameter

$$U = C_P \begin{cases} \rho_F^{p_1-1} & \text{for } \mu_0 \leq 1 \\ \rho_F^{p_2-1} \mu_0^{p_1-p_2} & \text{for } \mu_0 \leq 1 \end{cases} , \tag{15}$$

where $\rho_F = \sqrt{r_P/k}$, r_P is the BP propagation distance, $k = 2\pi f/c$, and $\mu_0 = \kappa_0 \rho_F$. From phase-screen equivalence the ordering property of U is expected to apply more generally. Figures 9, 10, and 11 summarize the segment $S4$ values from each site plotted against the U parameter computed with measured IPE and Fresnel scale parameters. If $S4$ values smaller than 0.25 are excluded, identical patterns are observed at the Hong Kong and Lampedusa sites. The PPB segments are shifted to larger U values, which is attributed to larger p_1 values. The associated Cp parameters are actually smaller. The Malandi pattern is evidently influenced by its proximity to the geomagnetic equator.
The fact the fewer small $S4$ EPB segments may be due to weaker delay phase structure being associated with single power law distributions.

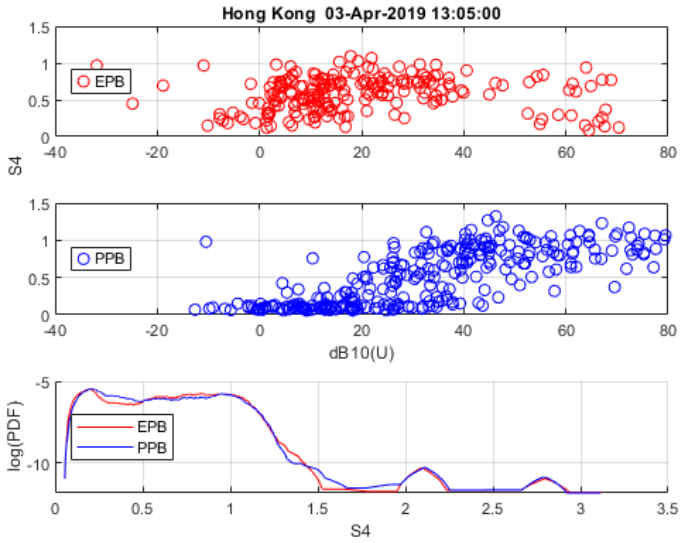

Figure 10: Upper frames show Hong Kong EPB and PPB S4 values plotted against the U parameter evaluated using IPE parameters and the BP Fresnel scale. The lower frame shows the PDFs capturing large S4 values not shown in the truncated display.

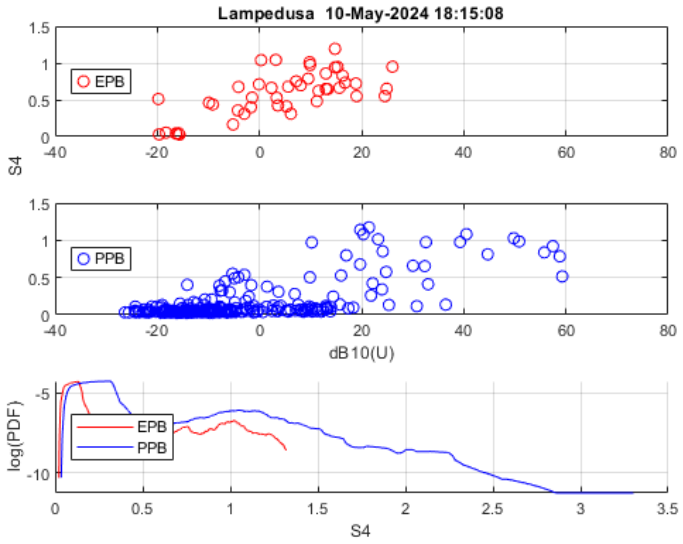

Figure 11: Lampedusa $S4$ summary.

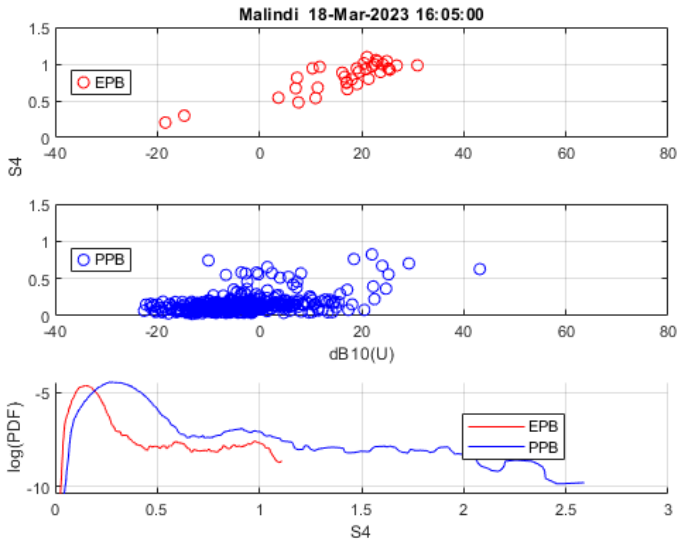

Figure 12: Malissa $S4$ Summary.

7 Summary and Discussion

A definitive structure analysis of low-latitude scintillation was performed by Xu et al. [6]. Their Figure 6 is the same summary presentation as the upper frames of Figures 9, 10, and 11. There is agreement. The disparity is Xu et al. [6] find no evidence of PPB structure. We suspect this is due to the fact that their IPE is applied to theoretical predictions of the intensity SDF that requires a scale-free limit that precludes enhances large-scale structure. In effect, the theoretical model can extract structure only over a power-law range that excludes PPB structure. The EPB structure with $p_1 < p_2$ and $p_1 < 3$ is well within the theoretic model range where the results agree. This needs further exploration. However, the IPE-BP analysis is identifying PPB structure that can be reproduced with MPS realizations.

Figure 13 summarizes a representative Hong Kong EPB segment. The upper frame shows the complex field intensity before (blue) and after (red) BP. There is very little change in $S4$, although the BP propagation distance change is significant. The middle frame shows the extracted and reconstructed phase range. Cycle slips account for the systematic differences. The large scale structure is largely unaffected. The lower frame shows the SDF with the noise estimate in blue. The extracted power-law parameters reproduce the SDF very well, which supports IPE integrity. Figure 14 summarizes an MPS simulation unsing the measured structure parameters with incremental phase applied over 40 km. The measured $S4$ value is realized at ~100 km. However, the is a 2π range ambituity that needs to be resolved.

Figures 15 and 16 show the same summary for a Hong Kong segment with PPB structure. The IPE parameters are derived with the same integrity as the EPB IPE parameters. The scintillation intensity levels are moderate with no indication of diffraction-induced errors. Moreover, there MPS simulations are simularly behaved. However, with $p2 > p1$ the theoretical phase screen SDF algorithm failed to converge illustrating the sensitivity of the algorithm to large-scale structure in the range that scale-free results suppress. Although there is clearly work to be done, the results support the existence of unexplained enhanced large scale structure that can dominate extreme scintillation.

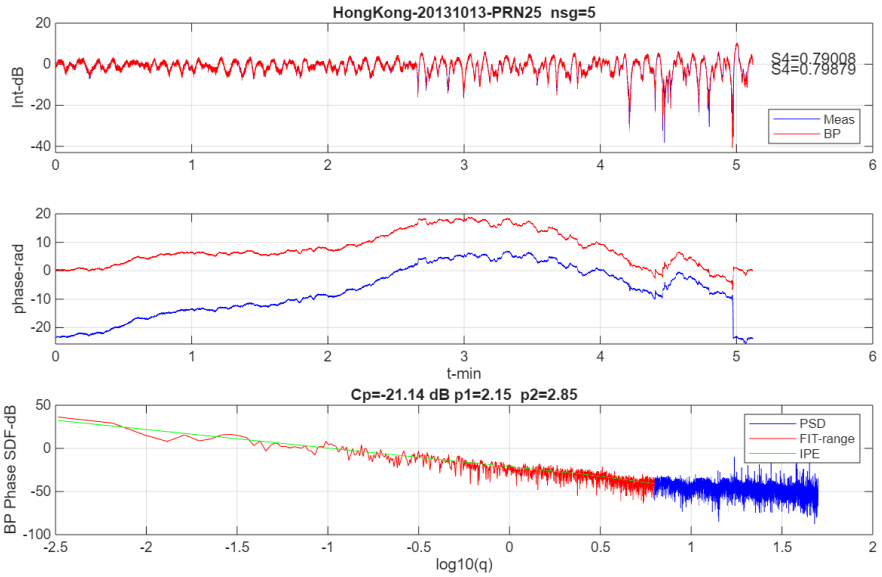

Figure 13: Hong Kong EPB segment BP-IPE structure summary. Top frame is intensity. Middle frame is phase. Lower frame is measured (red-blue) and IPE model SDF.

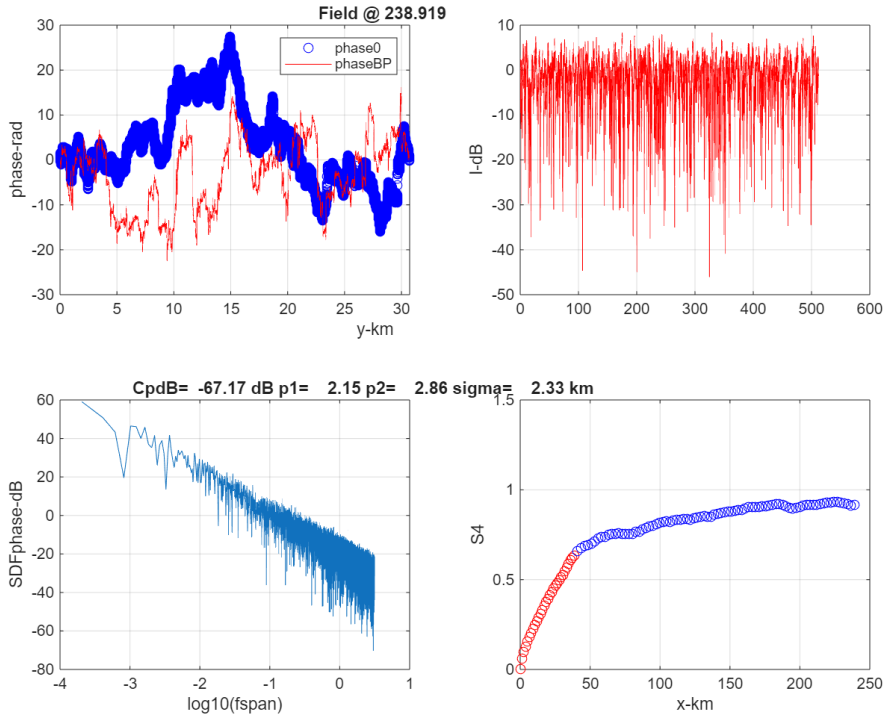

Figure 14: Summary of MPS simulation. SDF display fspan should be q.

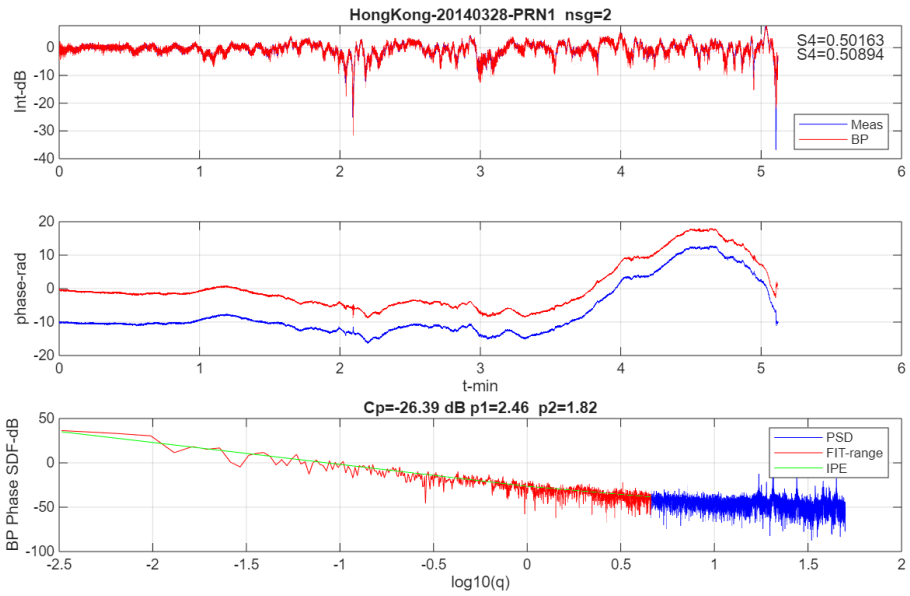

Figure 15: Hong Kong PPB segment BP-IPE structure summary. Top frame is intensity. Middle frame is phase. Lower frame is measured (red-blue) and IPE model SDF.

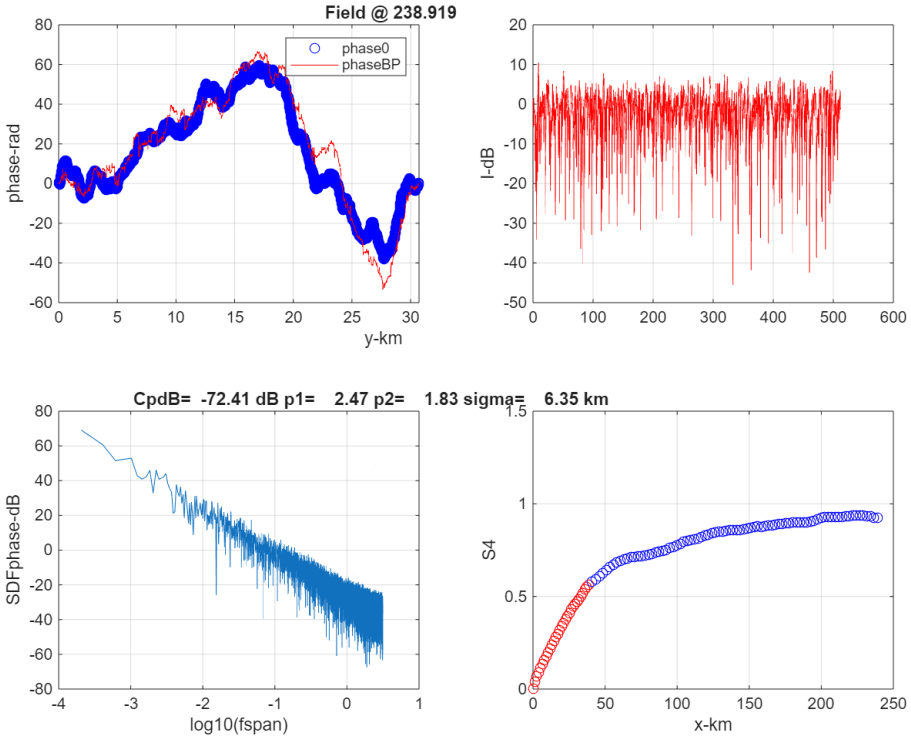

Figure 16: Summary of MPS simulation. SDF display fspan should be q.

References

[1] Charles Rino, Charles Carrano, Dmytro Vasylyev, Theodore Beach, Brian Breitsch, Yu Morton, and Keith Groves. Extreme scintillation structure diagnostics. *Journal of Atmospheric and Solar Terrestial Physics*, 282, 2026. https://doi.org/10.1016/j.jastp.2026.106805.

[2] C. Rino, C. Carrano, and K. Groves. Wave propagation in extended highly anisotropic media. *Radio Science*, 2019. doi:10.1029/2019RS006793.

[3] Ludwig-Barbosa1 VinÃŋcius, Joel Rasch, Thomas Sievert1, Anders CarlstrÃűm, Mats I. Pettersson, Viet Thuy Vu1, and Jacob Christensen. Detection and localization of f-layer ionospheric irregularities with the back-propagation method along the radio occultation ray path. *Atmospheric Measurement Technology*, 2023. doi.org/10.5194/amt-16-1849-2023.

[4] C. S. Carrano, C. L. Rino, and K. M. Groves. Maximum likelihood estimation of phase screen parameters from ionospheric scintillation spectra. *15th International Ionospheric Effects Symposium,Alexandria, VA, May 9-11*, pages 1–11, 2017.

[5] C Rino, C. Carrano, K. Groves, and T. Yokoyama. A configuration space model for intermediate-scale ionospheric structure. *Radio Science*, 53, 2018. 10.1029/2018RS006678.

[6] Dongyang Xu, Y.T. Jade Morton, Charles L. Rino, Charles S. Carrano, and Yu Jiao. A two-parameter multifrequency gps signal simulator for strong equatorial ionospheric scintillation: modeling and parameter characterization. *Navigation*, 2019. DOI: 10.1002/navi.350.